

# Nanoplasmonics simulations at the basis set limit through completeness-optimized, local numerical basis sets

Tuomas P. Rossi,<sup>1, a)</sup> Susi Lehtola,<sup>1, 2, b)</sup> Arto Sakko,<sup>1</sup> Martti J. Puska,<sup>1</sup> and Risto M. Nieminen<sup>1, 3</sup>

<sup>1)</sup> *COMP Centre of Excellence, Department of Applied Physics, Aalto University School of Science, P.O. Box 11100, FI-00076 Aalto, Finland*

<sup>2)</sup> *Chemical Sciences Division, Lawrence Berkeley National Laboratory, Berkeley, California 94720, USA*

<sup>3)</sup> *Dean's Office, Aalto University School of Science, P.O. Box 11000, FI-00076 Aalto, Finland*

(Dated: 11 October 2018)

We present an approach for generating local numerical basis sets of improving accuracy for first-principles nanoplasmonics simulations within time-dependent density functional theory. The method is demonstrated for copper, silver, and gold nanoparticles that are of experimental interest but computationally demanding due to the semi-core d-electrons that affect their plasmonic response. The basis sets are constructed by augmenting numerical atomic orbital basis sets by truncated Gaussian-type orbitals generated by the completeness-optimization scheme, which is applied to the photoabsorption spectra of homoatomic metal atom dimers. We obtain basis sets of improving accuracy up to the complete basis set limit and demonstrate that the performance of the basis sets transfers to simulations of larger nanoparticles and nanoalloys as well as to calculations with various exchange-correlation functionals. This work promotes the use of the local basis set approach of controllable accuracy in first-principles nanoplasmonics simulations and beyond.

## I. INTRODUCTION

Plasmonics attracts increasing interest due to its technological relevance in numerous applications, such as biochemical sensing,<sup>1</sup> sub-wavelength light manipulation,<sup>2</sup> and photovoltaics.<sup>3</sup> Plasmon resonances in metal nanoparticles can be qualitatively understood by classical electromagnetism, but the accurate description of nanometer-size particles or systems with features in the subnanometer range requires more elaborate approaches. In these systems the plasmonic response is affected by quantum effects, such as electron spill-out at the surface and electron tunneling.<sup>4</sup> A number of recent studies has demonstrated that the regime where these effects start to play a role is experimentally accessible.<sup>5–9</sup>

To study quantum effects in the plasmonic response computationally, one often resorts to time-dependent density functional theory<sup>10</sup> (TDDFT) simulations. Qualitative understanding on the quantum effects in nanostructures can be obtained within the jellium approximation,<sup>11–14</sup> but it cannot capture the important atomic structure effects.<sup>15</sup> In addition, the jellium model only describes simple metals such as sodium, where the optical response is determined by the valence s-electrons. However, the experimentally relevant materials for plasmonics are usually coinage metals; copper (Cu), silver (Ag), and gold (Au).<sup>5–9, 16, 17</sup> In these metals, in addition to the outermost s-electrons, also the semi-core d-electrons participate in the response. Although the effects due to the d-electrons can be accounted for

in an approximate manner in the jellium model,<sup>18</sup> first-principles models are necessary to obtain accurate results.

Coinage metal systems have been studied through numerous TDDFT simulations, including metal nanoparticles of different shapes,<sup>19–26</sup> nanoalloys,<sup>27–31</sup> protected metal clusters,<sup>32–36</sup> and nanoparticle dimers.<sup>37</sup> However, TDDFT simulations for these systems are computationally demanding. Even though the calculations can be speeded up with the frozen-core approximation, coinage metals require explicit calculation of the semi-core d-electrons in addition to the s-electrons, resulting in 11 electrons per atom in calculations, in contrast to, *e.g.*, sodium where it usually suffices to treat only the single 3s-electron per atom. Consequently, simulated systems have typically been restricted to the maximum size range of 100–200 coinage metal atoms,<sup>19–23, 27–33, 35–37</sup> with a few studies presenting larger systems, such as a Au<sub>263</sub> nanorod,<sup>26</sup> a Ag<sub>272</sub> nanoshell,<sup>24</sup> and a thiolate-protected Au<sub>314</sub>.<sup>34</sup> The calculations have employed either real-space grid codes<sup>26–28, 33–36</sup> or the linear combination of atomic orbitals (LCAO) approach.<sup>19–24, 29–32, 37</sup> Recently, a new LCAO-TDDFT implementation was developed,<sup>25</sup> allowing to push the accessible system size close to the classical limit (Ag<sub>561</sub> presented in Ref. 25).

A serious problem of the LCAO approach is that it is prone to errors due to basis set incompleteness — a problem which can be straightforwardly tackled in the real-space grid methods. Nevertheless, this issue has not been extensively discussed in previous nanoplasmonics studies using the LCAO approach. Instead, a reasonable accuracy of the results has been checked by calculations of test systems with larger basis sets of the available basis set series<sup>19, 20, 24</sup> or by comparing to real-space grid results.<sup>25</sup>

<sup>a)</sup> Electronic mail: [tuomas.rossi@alumni.aalto.fi](mailto:tuomas.rossi@alumni.aalto.fi)

<sup>b)</sup> Electronic mail: [susi.lehtola@alumni.helsinki.fi](mailto:susi.lehtola@alumni.helsinki.fi)

The basis set issue is complicated by the fact that conventional basis sets are typically optimized for ground-state energy calculations.<sup>38</sup> For other properties, such as dipole moments, excited states, or plasmonic charge density oscillations, these basis set series are not expected to yield quickly converging results.<sup>39–43</sup> In the case of photoabsorption spectra, the accurate description of the dipole moment of the excited states is essential. This necessitates inclusion of diffuse functions (*i.e.*, functions with large spatial extent) in the basis set. Diffuse functions are not present in the energy-optimized basis sets because of their minor contribution to the ground-state energy of electrically neutral systems, but they can be generated into these basis sets by, *e.g.*, minimizing the energy of anions.<sup>38</sup> Alternatively, unoccupied atomic orbitals can be included in the basis set, which has been found to improve the description of the photoabsorption of metal nanoparticles.<sup>25,44</sup> However, these approaches are not guaranteed to be optimal for extending the basis sets beyond conventional ground-state energy calculations.

In the present work, we show that efficient basis sets specifically optimized for describing the plasmonic optical response can be systematically generated using the completeness-optimization (CO) approach.<sup>41</sup> CO is a black-box procedure for generating basis sets for any property at any level of theory. It has been previously used to generate all-electron Gaussian-type orbital (GTO) basis sets for calculating magnetic<sup>41,45–50</sup> and magneto-optic<sup>51–57</sup> properties as well as the electron momentum density.<sup>42,58</sup> In this work, we present a straightforward extension of the CO formalism to semi-numerical basis sets by combining numerical atomic orbitals (NAOs) with truncated numerical Gaussian-type orbitals (NGTOs). The NGTOs are selected by a recently developed automatic CO procedure<sup>42,43</sup> to augment NAO basis sets with the necessary diffuse and polarization functions. We demonstrate the applicability of the scheme for describing collective plasmonic excitations in coinage metal clusters. We optimize the basis sets to reproduce the photoabsorption spectra of homoatomic dimers, and show that the generated basis sets are transferable to larger nanoparticles and to different chemical environments in nanoalloys, as well as to different exchange-correlation functionals.

The paper is organized as follows. In Sec. II, we give an overview of the used methodologies — TDDFT, LCAO, and CO. In Sec. III, we describe our implementation, and in Sec. IV we demonstrate the performance of the basis set generation and test the transferability of the generated basis sets. We conclude the study in Sec. V.

## II. METHODS

### A. Time-dependent density functional theory

TDDFT is a well-established formulation of the time-dependent many-body Schrödinger equation in terms of

the time-dependent electron density.<sup>10</sup> The theory is usually applied within the Kohn–Sham (KS) description of density functional theory (DFT),<sup>59,60</sup> which models the interacting many-electron system as a non-interacting system in an effective potential. In this approach, the complicated many-body interactions are described by the so-called exchange-correlation (xc) functional. The time-dependent xc functionals are usually treated in the adiabatic limit, *i.e.*, an instantaneous time-dependent density is used as input for the ground-state functional.<sup>61</sup>

The dynamical response, and in particular, the photoabsorption spectrum of a given system, can be calculated in two formally different, but equivalent manners within the TDDFT framework. First, it can be obtained from the time-dependent dipole moment that is recorded during the explicit real-time propagation of the KS-orbitals that have been excited from the ground state by a  $\delta$ -pulse perturbation.<sup>62</sup> Second, the excitations of the system can be calculated by formulating the linear density response to an external perturbation in the frequency space, yielding the Casida matrix equation.<sup>63</sup>

In this work, we use both the time-propagation and Casida schemes for calculating photoabsorption spectra. We employ the open source GPAW program<sup>64–69</sup> in TDDFT calculations. GPAW uses the projector augmented wave (PAW) method<sup>70</sup> for freezing the inert core electrons and for obtaining smooth pseudo-wave functions in the vicinity of the nuclei. The simulations explicitly include only the outermost electrons, *i.e.*, for the coinage metals, the semi-core d-electrons and the valence s-electrons (11 electrons per atom in total). The element-specific PAW transformations are constructed at the scalar-relativistic level of theory. Thus, relativistic effects, especially important for gold,<sup>71</sup> are included implicitly in the calculations through the PAW transformation. For the present study, GPAW has the advantage that it can describe wave functions either on a real-space grid<sup>64,65</sup> or within the LCAO approach.<sup>25,66</sup> In both modes, uniform real-space grids are used for representing electron densities and potentials. These two modes of operation share a significant portion of computational framework within the program, which allows us to compute grid-based spectra and LCAO spectra with minimal sources of differences apart from the representation of the wave functions.

### B. Linear combinations of atomic orbitals

In the LCAO approach the single-electron KS wave function is expressed as

$$|\psi\rangle = \sum_a^{\text{atoms}} \sum_{\nu=1}^{N_a} c_{\nu}^a |\chi_{\nu}^a\rangle, \quad (1)$$

where  $c_{\nu}^a$  are the expansion coefficients for basis functions  $|\chi_{\nu}^a\rangle$  centered on the atom  $a$ ,  $N_a$  denoting the amount of basis functions on that atom. In a coordinate system

centered on the atom  $a$ , an associated basis function is written as a product of a radial function  $\phi_{nl}^a(r)$  and a spherical harmonic  $Y_{lm}(\theta, \varphi)$ ,

$$\langle \mathbf{r} | \chi_\nu^a \rangle = \chi_\nu^a(\mathbf{r}) = \phi_{n_\nu l_\nu}^a(r) Y_{l_\nu m_\nu}(\theta, \varphi). \quad (2)$$

Above,  $\nu$  is a symbolic index over the combinations of  $n_\nu$ ,  $l_\nu$ , and  $m_\nu$ . In this work, radial functions are taken to be either NAOs or NGTOs as described in Sec. III.

The main advantage of the LCAO approach is that a sufficiently accurate description of the wave function can often be achieved with a small number of basis functions. In addition, in the case of truncated basis functions, the number of overlapping basis functions is usually small, which enables efficient computations. The main drawback of the LCAO approach is that it is prone to errors due to the incompleteness of the basis set. Thus, it is important to use basis sets that are flexible enough for describing wave functions accurately in the regions that are essential for the property in question.

### C. Completeness-optimization

CO is a general approach for generating optimal basis sets for any chosen property.<sup>41</sup> The method is based on the concept of the completeness profile<sup>40</sup> that is defined as

$$Y_l(\alpha) = \sum_{\mu, \nu=1}^N \langle g_l(\alpha) | \chi_\mu \rangle S_{\mu\nu}^{-1} \langle \chi_\nu | g_l(\alpha) \rangle, \quad (3)$$

where  $|\chi_\nu\rangle$  are the basis functions,  $S_{\mu\nu}^{-1}$  is the  $(\mu, \nu)$  element of the inverse overlap matrix orthonormalizing the basis, and  $g_l(\alpha)$  is a primitive test function usually taken to be a normalized Gaussian primitive  $g_l(\alpha) \propto r^l e^{-\alpha r^2} Y_{lm}(\theta, \varphi)$ . For basis functions of the form of Eq. (2), the inner product  $\langle g_l(\alpha) | \chi_\nu \rangle \propto \langle r^l e^{-\alpha r^2} | \phi_{n_\nu l_\nu} \rangle \delta_{l_\nu l} \delta_{m_\nu m}$ . Thus, each value of the angular momentum  $l$  yields a different completeness profile  $Y_l(\alpha)$ , whereas all  $m$  values of a given  $l$  yield the same profile.

The profile essentially measures the validity of the resolution of the identity operator

$$\sum_{\mu, \nu=1}^N |\chi_\mu\rangle S_{\mu\nu}^{-1} \langle \chi_\nu| \approx \mathbb{I}, \quad (4)$$

which would be exact for a complete basis set. Correspondingly, the completeness profile satisfies  $0 \leq Y_l(\alpha) \leq 1$ .

The idea in CO is to generate a basis set that has  $Y_l(\alpha) \approx 1$  within the intervals  $[\alpha_l^{\min}, \alpha_l^{\max}]$  that are important for the property in question. This is accomplished by optimizing the parameters of the basis functions so that  $Y_l$  is maximized within the intervals. The number of basis functions needed for this depends on the tolerance  $\tau_l$  for deviations from unity in  $Y_l$  within the intervals.<sup>41–43</sup> The task of a practical CO algorithm is

to find the optimal limits of the intervals, while keeping  $Y_l(\alpha) \approx 1$  within the intervals.

In this work, we use Gaussian basis functions characterized by their exponents  $\alpha$  and employ the automatic CO procedure<sup>42,43</sup> implemented in the open source ERKALE program.<sup>72,73</sup> The procedure is based on systematic trial and error searches for determining the complete basis set (CBS) limit of the property, as well as the CBS itself. The algorithm is divided in two phases. First, in the extension phase, the CBS is found by progressively extending the basis set with the *most important* functions until the property is converged. Each addition of a basis function corresponds to an extension of the intervals  $[\alpha_l^{\min}, \alpha_l^{\max}]$  or decrease of the tolerance  $\tau_l$ . Second, in the reduction phase, the *least important* basis functions are repeatedly pruned from the basis, shrinking the  $\alpha_l$  intervals or increasing  $\tau_l$ . During the optimization, the relative importance of the addition or removal of a basis function is determined by a user-defined error metric. In every step of the algorithm, the exponents of the Gaussian basis functions are determined by maximizing the completeness profile  $Y_l$  within the current  $\alpha_l$  interval. As a result of the reduction phase, a systematic sequence of basis sets of decreasing size and accuracy is obtained.

## III. IMPLEMENTATION

### A. Application of the completeness-optimization in nanoplasmonics

The CO routine<sup>43</sup> has a general interface for basis set generation. We have written a wrapper program that implements this interface and calls the GPAW program<sup>68</sup> for photoabsorption spectrum calculations. The practical workflow between the programs is as follows. The optimization routine forms trial GTO basis sets and feeds them to the wrapper. The wrapper transforms the GTO sets into NGTOs, prepares the input for GPAW, and submits the GPAW calculations. Once the GPAW jobs have completed, the wrapper reads in the results and returns them to the optimization routine, which interprets them through the error metric and uses the information to update the basis set and generate new trials.

The error metric for determining the effect of modifying the basis set is defined as follows. The error  $\epsilon$  of a photoabsorption cross-section  $\sigma_{\text{abs}}(\omega)$  from the corresponding reference spectrum  $\sigma_{\text{abs}}^{\text{ref}}(\omega)$  (given by an earlier CO step) is defined as

$$\epsilon = \min_{\delta} \left[ \frac{\left( \int_{\omega_{\min}}^{\omega_{\max}} |\sigma_{\text{abs}}(\omega - \delta) - \sigma_{\text{abs}}^{\text{ref}}(\omega)|^2 d\omega \right)^{1/2}}{\left( \int_{\omega_{\min}}^{\omega_{\max}} |\sigma_{\text{abs}}^{\text{ref}}(\omega)|^2 d\omega \right)^{1/2}} + e^{(\delta/\gamma)^2} - 1 \right], \quad (5)$$

where  $\omega_{\min}$  and  $\omega_{\max}$  are cut-off energies,  $(e^{(\delta/\gamma)^2} - 1)$  is

a penalty term for a constant energy shift  $\delta$  in the spectrum, and  $\gamma$  describes the stiffness of the penalty function. The error metric also depends implicitly on the parameters used to broaden the discrete TDDFT spectrum to model the finite lifetime of excitations as well as temperature effects and instrumental resolution. Without explicitly allowing an energy shift  $\delta$  in the definition, the error measure would be much more sensitive to offsets in energy than to changes in intensity. The energy shift  $\delta$  is penalized through the penalty term, in which the parameter  $\gamma$  provides a sliding scale to balance the sensitivity of the measure between energy and intensity. With  $\gamma \rightarrow 0^+$  the penalty term becomes extremely stiff and  $\delta = 0$  always minimizes the error metric, in which case the metric becomes the usual normalized  $L^2$  measure. The error metric is also used for benchmarking the quality of the obtained basis sets. In this case, the reference spectrum is obtained from a real-space grid calculation. However, it is emphasized that during the optimization the grid reference is not employed by any means.

A practical issue concerning the extension of the CO routine to the frozen-core approximation is that the CO routine was initially designed for all-electron calculations. In the present work, the basis sets only represent the outermost s- and d-electrons of the coinage metal atoms, as the core electrons are described implicitly. Thus, the assumptions made for the composition of the basis set in the all-electron case<sup>43</sup> have been relaxed here, allowing for a non-monotonic amount of GTOs on consecutive angular momentum shells during basis set reduction.

## B. NAO+NGTO basis sets

The benefit of NAOs is that they are not restricted to be of any analytical form. Thus, they should excel in the highly structured atomic core region, which is only slightly affected by the surrounding chemical environment. Although the PAW transformation results in a smoother pseudo-wave function in this region, the NAOs are still pre-eminent for describing the atomic ground state.

While the generation of minimal-basis NAOs is straightforward, the case for polarization and multiple- $\zeta$  functions is not as clear. NAOs do not hold advantages for these functions, as the forms of the functions are not generally known and the polarization changes from one system to the other. NAO polarization and multiple- $\zeta$  functions are typically generated from gas-phase atomic wave functions by splicing the radial function<sup>74</sup> and/or by including bound unoccupied orbitals, but also other systematic approaches for generating NAO basis sets have been developed.<sup>75-78</sup> Here, (N)GTOs have a definite advantage, as systematic sets of functions of any angular momentum can easily be generated. In the default basis sets of GPAW, NGTOs are employed in addition to numerical orbitals and splicing.<sup>66</sup>

We employ the following strategy for basis set gener-

ation. NAOs are used to represent the atomic ground state, for which they hold the definitive advantage. This minimal basis is then augmented with NGTOs that are generated by the CO routine, adding the desired polarization and diffuse functions.

The CO routine treats analytical GTOs, whereas in this work, numerical basis functions are used. Thus, the analytical GTOs are smoothly truncated to NGTOs in the wrapper program by a second-order polynomial so that the radial part becomes

$$G(r) = Ar^l(e^{-\alpha r^2} - (a - br^2)), \quad (6)$$

where  $A$  is a normalization constant, and the constants  $a$  and  $b$  are chosen so that  $G(r_c) = G'(r_c) = 0$  at the cut-off radius  $r_c$ .<sup>79</sup> The cut-off radius is determined by requiring that the NGTO differs point-wise from the exact GTO  $\propto r^l e^{-\alpha r^2}$  at most by  $10^{-3}$  au<sup>-3/2</sup>. This strict criterion distorts the Gaussian shape negligibly, but, on the other hand, leads to large  $r_c$  values, which has a detrimental effect on the computational cost.

Because of the negligible difference between GTOs and NGTOs, the analytical form is used in the optimization of the Gaussian primitives, *i.e.*, in the maximization of the completeness profile Eq. (3) determining the exponents of the primitives. Additionally, the underlying NAOs are neglected in Eq. (3). Although NAOs (and truncated NGTO forms) could be straightforwardly included in the optimization of the completeness profile (Eq. (3)), the effects due to the explicit account of the NAOs at this stage are expected to be small due to the different asymptotic forms of NAOs and GTOs. The incorporation of the underlying NAO basis set is done in the wrapper program so that its presence is invisible to the CO routine and the major effect of NAOs rises implicitly through the spectrum calculation.

The following *ad hoc* restrictions are imposed for the allowed NGTOs. At least 90% of the norm of the function must be within a sphere of radius 6 Å around the nucleus and at most 90% of the norm may be within 0.6 Å.<sup>80</sup> The first condition results in the rejection of extremely diffuse functions that would require impractically large simulation grids, and which would cause severe numerical problems due to linear dependencies in extended systems. The second condition ensures that even the tightest functions can be faithfully mapped to the real-space grid used to describe their contributions to the electron density. However, tight functions are not usually needed anyhow because of the PAW transformation.

## C. Numerical parameters

The CO was started from an initial NAO+NGTO basis set composed of three radial functions on the s-, p-, and d-shells, totaling 27 basis functions per atom. The initial GTO basis set was energy-optimized<sup>43</sup> for the gas-phase atom in question. The value  $\gamma = 0.4$  eV was used

in the error metric (Eq. (5)) during the CO, and the spectra were broadened with Gaussians using a full width at half maximum (FWHM) of 0.47 eV. The FWHM and  $\gamma$  parameters used in the CO were determined by trial and error to obtain a suitable balance between the energy and intensity sensitivities. The parameters were not specifically optimized and other values that achieve a proper balance are expected to yield similar results. For the integration limits,  $\omega_{\min} = 0$  eV was used, and  $\omega_{\max}$  was set to 5.2 eV, 5.4 eV, and 6.7 eV for  $\text{Cu}_2$ ,  $\text{Ag}_2$ , and  $\text{Au}_2$ , respectively. The  $\omega_{\max}$  limits were estimated from the grid-reference calculations so that spurious box-state transitions are excluded. The same parameters are also used in Sec. IV A for calculating the errors with respect to the grid reference. The extension phase was terminated when the error between consecutive spectra was smaller than 0.011. The maximum angular momentum in the basis set was set to  $l = 3$ , allowing for s-, p-, d-, and f-type GTOs to be generated by the algorithm. The effect of higher- $l$  basis functions is expected to be insignificant.

The LCAO spectra of homoatomic dimers were calculated within Casida’s linear-response TDDFT formalism<sup>63</sup> by including the full eigenstate spectrum corresponding to the finite basis set and averaging over the longitudinal and transversal components. Other systems and all grid references were calculated with time-propagation TDDFT<sup>62</sup> using a weak  $\delta$ -pulse and a time step of 10 as. The Perdew-Burke-Ernzerhof (PBE) xc functional<sup>81,82</sup> in the adiabatic limit was used in all the calculations, unless otherwise stated. All the calculations were done as spin-paired. The following GPAW-specific parameters were used. LCAO mode: grid spacing  $h = 0.3$  Å and minimal vacuum size around the system  $d_{\text{vac}} = 6$  Å. Grid mode:  $h = 0.25$  Å and  $d_{\text{vac}} = 8$  Å. The accuracy of the Hartree potential evaluation within the simulation cell was improved by employing multipole corrections to the potential.<sup>83</sup> The grid mode uses the real-space grid for describing the wave functions, which explains the smaller  $h$  and larger  $d_{\text{vac}}$  values needed for converged results. In the LCAO mode, the numerical basis functions are described on their specific radial grids and the uniform real-space grid is used only for representing the density and potentials.<sup>66</sup>

In the transferability tests (see Secs. IV B–IV D), the spectra were convoluted by a Gaussian broadening with FWHM = 0.20 eV. The value  $\gamma = 0.25$  eV was used in the error metric to obtain a reasonable energy/intensity sensitivity. These parameters yield the same error for a spectrum shift of 0.1 eV and an intensity change by 20% for a test spectrum with a single absorption peak. The integration limits in the error metric were set to  $\omega_{\min} = 0$  eV and  $\omega_{\max} = 5$  eV to probe the visible–near-UV region of spectrum.

## IV. RESULTS

### A. Generation of basis sets

The basis sets were generated independently for Cu, Ag, and Au by using the photoabsorption spectrum of the corresponding homoatomic metal atom dimer as the completeness-optimization target. The dimer bond lengths were optimized with GPAW by using the default dzp basis sets and the PBE functional. The obtained bond lengths for  $\text{Cu}_2$ ,  $\text{Ag}_2$ , and  $\text{Au}_2$  are 2.23 Å, 2.58 Å, and 2.55 Å, respectively. The used values agree well with the experimental values, 2.22 Å, 2.53 Å, and 2.47 Å, respectively.<sup>84</sup>

The progression of the CO procedure for the silver dimer is illustrated in Fig. 1 for different choices of the underlying NAO basis sets. In the extension phase, the error in the LCAO calculation decreases rapidly. Once the complete basis set (CBS) limit has been reached, the least-important primitives are pruned out one by one in the reduction phase. During many sequential steps, the reduction-phase basis sets yield more accurate results with less basis functions than the ones from the extension phase. The progression of the algorithm is not completely monotonic, because the optimized property is not variational.<sup>43</sup>

For the rest of the work, we focus on the NAO-sz+NGTO basis sets.<sup>85</sup> Then, only a minimal NAO basis set is included, so that CO produces all the polarization functions necessary for describing the chemical ground-state environment as well as the excited state charac-

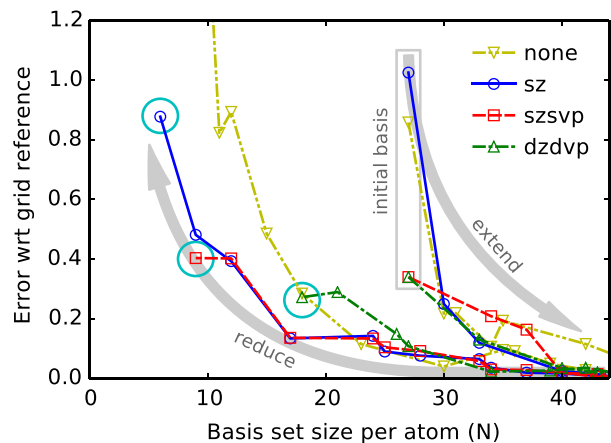


FIG. 1. The progression of the CO procedure for  $\text{Ag}_2$  during the extension and reduction phases as illustrated by the error with respect to the grid-calculated reference spectrum (Eq. (5)). Different underlying NAO basis sets are used: 1) “none”: only NGTOs, 2) “sz”: single- $\zeta$  basis of 4d and 5s orbitals, 3) “szsvp”: single- $\zeta$  basis of 4d, 5s, and 5p orbitals, 4) “dzdvp”: double- $\zeta$  basis of 4d, 5s, and 5p orbitals. The cyan circles mark the NAO-only basis sets.

teristics. Contrary to NAO-only basis sets, the NAO-sz+NGTO basis sets are completely general. The occupied orbitals used in the NAO-sz basis can be generated for any element, whereas the first unoccupied orbitals may not be bound, in which case they cannot be directly included. Additionally, the comparison between “sz” and “szsvp” reduction series in Fig. 1 indicates that the use of the unoccupied p-orbital in the NAO basis does not result in a large difference, at least for the silver dimer.

Furthermore, the NAO-sz+NGTO basis sets are expected to be numerically efficient. We note from Fig. 1 that these basis sets indeed perform better than either the NAO-dzdv+NGTO sets or the pure NGTO sets. The reasons are that the NAO-dzdv basis sets contain extra NAO functions, which are not free to be optimized by the CO method, and that the pure NGTO basis sets do not have the advantage of the minimal NAO-sz basis sets. However, the NAO basis sets depend on the used xc functional whereas the pure NGTO basis sets could be more transferable across different functionals. Still, the underlying NAOs can be easily changed with the functional. This approach is presented in Sec. IV D.

To illustrate the generated basis sets, we present two NAO-sz+NGTO basis sets for Cu, Ag, and Au in Fig. 2. The basis sets with  $N = 17$  are expected to yield decently accurate results (see Fig. 1) and the  $N = 36 / N = 37$  ones are close to the CBS limit. Henceforth, we refer to the  $N = 17$  basis sets as “CO-1” and the  $N = 36 /$

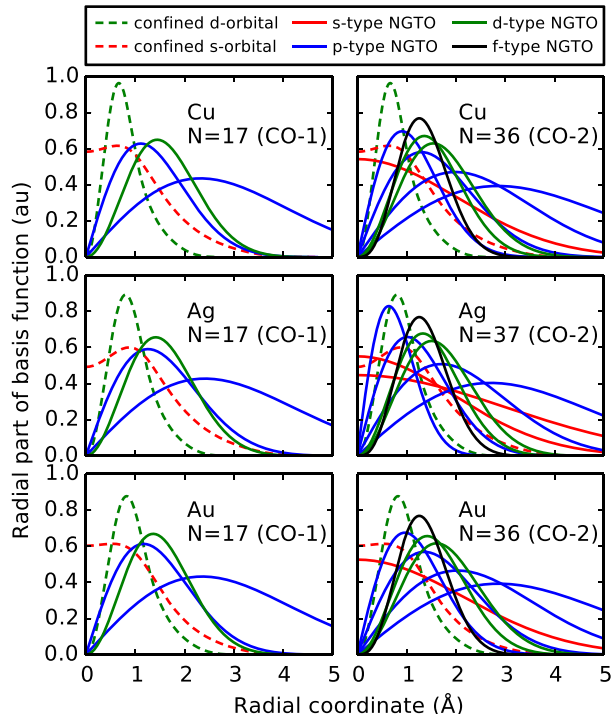


FIG. 2. NAO-sz+NGTO basis sets generated by the CO algorithm. Basis sets with 17 and 36 or 37 functions for Cu, Ag, and Au are shown.

$N = 37$  basis sets as “CO-2”. The similarity of the basis sets across the studied elements is evident. In the CO-1 basis sets, the NAO-sz basis is augmented by two diffuse p-type NGTOs and a single d-type NGTO. In the CO-2 case, additional NGTOs are included on all shells. The Gaussian exponents of the NGTOs are similar across all studied elements, which is expected due to their closely related chemical characteristics. Yet, even though the shown basis sets are similar for all elements, the whole basis set *series* are not the same, as functions are pruned out in different orders in the reduction phase. For example, there is no  $N = 36$  basis set for silver. Note also that the most diffuse p-type NGTOs are at the constraint limit imposed for NGTOs (see Sec. III B).

## B. Transferability of basis sets to larger clusters

The usefulness of basis sets depends on their transferability to different chemical environments. Here, we consider the transferability of the basis sets obtained in the previous section to larger systems by using homoatomic icosahedral clusters of 13, 55, and 147 atoms as test cases. The clusters were constructed by adding icosahedral Mackay layers one by one around a central atom. The structures were relaxed with GPAW by using the default dzp basis sets and the PBE functional, but their icosahedral symmetries were not significantly disturbed.<sup>85</sup>

We show in Fig. 3 the error in the photoabsorption spectra (Eq. (5)) for the clusters. We observe a nearly monotonic increase in the accuracy with increasing basis set size. The magnitude of the error is similar between different elements, and the error tends to decrease when the system size increases.

In Fig. 3, we also show for comparison the errors of the GPAW default dzp basis set and the NAO-dzdv basis set that has been used in a previous study.<sup>25</sup> The default dzp basis set is unsuitable for describing the response, which is due to its lack of diffuse p-functions.<sup>25</sup> The NAO-dzdv basis set provides an equivalent or better accuracy than the NAO-sz+NGTO basis set of similar size. However, in contrast to the NAO-only basis sets, the basis sets generated in the present work allow for further, systematic improvements in accuracy beyond that of the NAO-only basis sets.

The insets in Fig. 3 illustrate how the spectra look for the 55-atom clusters calculated with basis sets of different size. We observe that all the spectral features are mostly correct with the basis sets of 17 or more functions per atom. The CO-1 spectra suffer from a blue-shift of 0.1–0.2 eV and the largest improvement in the spectrum when growing the size of the basis set comes from a red-shift towards the converged spectrum. The CO-2 basis sets of Cu and Ag are already at the CBS limit, as the positions of the spectral peaks coincide with the grid references within 0.05 eV. For Au, the convergence is slow after  $N \approx 24$ , but also there the CO-2 spectrum is near the grid reference except for a few details.

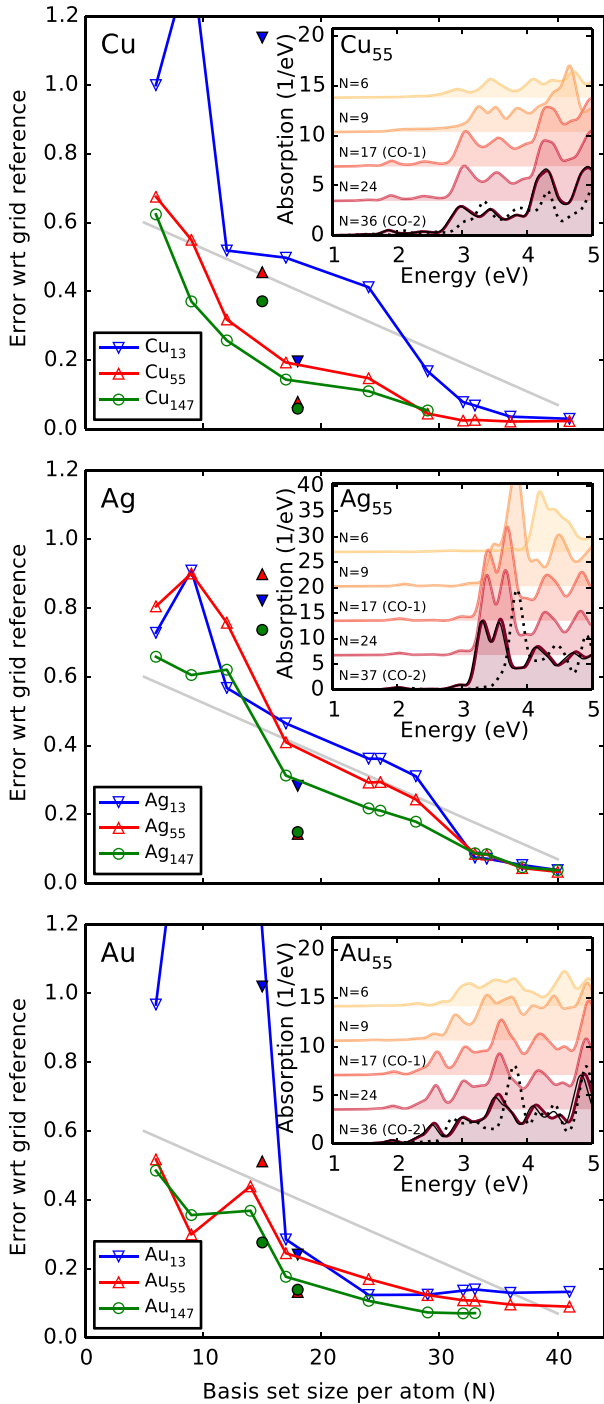


FIG. 3. Transferability of the generated NAO-sz+NGTO basis sets to icosahedral homoatomic coinage metal clusters of 13, 55, and 147 atoms. The off-line filled markers indicate results calculated with the GPAW default dzp ( $N = 15$ ) and NAO-dzdvp basis sets ( $N = 18$ ). The straight gray line is drawn to ease the visual comparison. The insets present photoabsorption spectra of 55-atom clusters calculated with basis sets of increasing size. The grid reference (thin black line) and the LCAO spectrum with the default dzp basis (dotted line) are also shown in the insets.

### C. Transferability of basis sets to nanoalloys

Now, we consider the transferability of the basis sets that were optimized for homoatomic dimers to heterogeneous metal clusters, where the chemical environments are different from the homogeneous systems. As test systems, we take the core-shell clusters  $\text{Ag}_{13}\text{Cu}_{42}$ ,  $\text{Cu}_{13}\text{Ag}_{42}$ ,  $\text{Ag}_{13}\text{Au}_{42}$ , and  $\text{Au}_{13}\text{Ag}_{42}$ , which consist of icosahedral 13-atom cores and single 42-atom Mackay layers around the cores, as well as two icosahedral alloys,  $\text{Cu}_{14}\text{Ag}_{20}\text{Au}_{21}$  and  $\text{Cu}_{18}\text{Ag}_{17}\text{Au}_{20}$ , which were generated by random substitution of atoms in the 55-atom icosahedral geometry. The clusters were relaxed analogously to the homoatomic clusters in Sec. IV B.<sup>85</sup>

The photoabsorption spectra of the alloy clusters are shown in Fig. 4. The CO-2 spectra are again in excellent agreement with the grid reference. The smaller CO-1 basis set results in a 0.1–0.2 eV blue-shift of the spectra. Due to the lower symmetry and breaking of degeneracies the disordered clusters have fewer sharp spectral features than the core-shell clusters. This is also reflected in that only small differences between the CO-1 and CO-2 spectra can be seen.

The spectra calculated with the default dzp basis sets are also shown in Fig. 4. As in the case of homoatomic clusters, these basis sets are unable to sufficiently describe the photoabsorption spectra. The trends in the results obtained with the NAO-dzdvp basis sets (not shown) are similar to those in the homoatomic case.

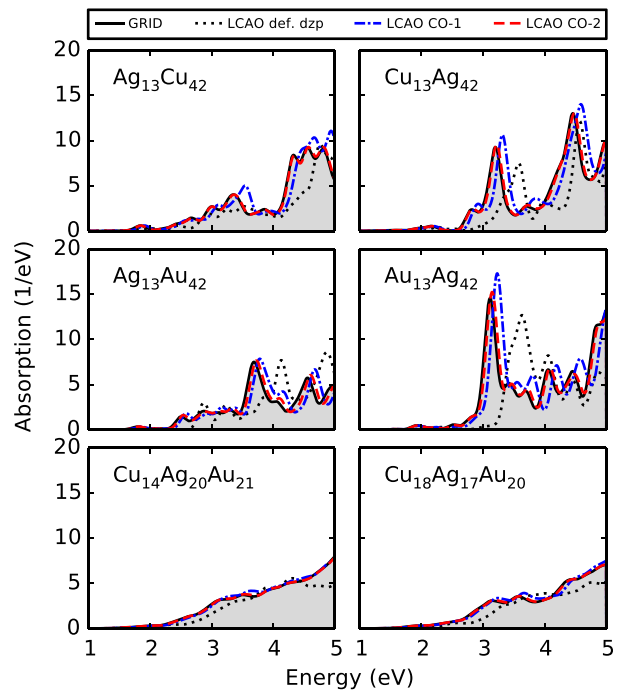


FIG. 4. Transferability of the basis sets to alloy clusters. The gray shading is applied to the grid-reference spectra.

#### D. Transferability of basis sets to different xc functionals

Different xc functionals yield different shapes of the KS-orbitals. We studied how the generated NGTOs transfer across various xc functionals. The basis sets were constructed by augmenting the NAO-sz basis set corresponding to the chosen functional with the PBE-optimized NGTOs without any further modification. We used the  $\text{Ag}_{55}$  cluster as the test system. The results for the local density approximation (LDA),<sup>86–88</sup> the Becke-Lee-Yang-Parr (BLYP) functional,<sup>89–91</sup> and the solid-state modification of the Gritsenko-van Leeuwen-van Lenthe-Baerends potential (GLLB-SC)<sup>92,93</sup> are shown in Fig. 5, where also the PBE results of Fig. 3 are repeated for reference. While the LDA, PBE, and BLYP functionals predict similar spectra, the GLLB-SC spectrum has a distinct shape and stronger intensity. This is due to the d-electron screening in coinage metals that is captured correctly by the GLLB-SC functional.<sup>25,94,95</sup> The default dzp basis sets, shown for comparison in Fig. 5, reproduce the strong intensity difference between the GLLB-SC and the other functionals but are inadequate to describe the detailed structure of the spectra, failing to agree with the grid references. In contrast, the CO-1 basis sets mostly capture the detailed differences between the xc functionals, and the accuracy of the CO-1 basis sets is similar with all the studied functionals. The CO-2 results are again in excellent agreement with the grid references in all cases. Altogether, the results illustrate notable transferability of the PBE-optimized CO basis sets to diverse xc functionals.

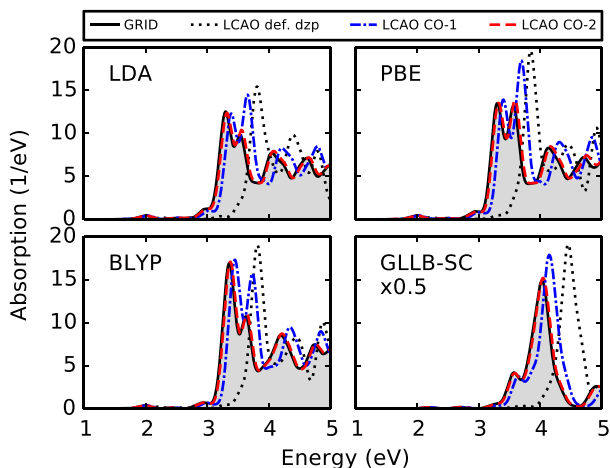


FIG. 5. Transferability of the PBE-optimized basis sets to different xc functionals. Results for  $\text{Ag}_{55}$  are shown. The GLLB-SC spectrum has been multiplied by a factor of 0.5. The gray shading is applied to the grid-reference spectra.

#### E. Computational performance

A major advantage of LCAO calculations is that their computational cost is smaller than that of, *e.g.*, real-space grid calculations. However, the advantage decreases if large basis sets must be used. To understand this important issue, we discuss the effect of basis set size on the computational cost. Fig. 6 presents the time-propagation run-times of the generated basis sets as calculated for the  $\text{Ag}_{55}$  and  $\text{Ag}_{147}$  clusters with 48 and 96 processors (cores).<sup>96</sup> Depending on the case, enlarging the basis set from CO-1 to CO-2 (*i.e.*, from  $N = 17$  to  $N = 37$ ) increases the computational cost by a factor of 2 to 5.

The CO-2 calculations are still 5 to 8 times faster than the grid-reference calculations, while the differences between the results are minimal as observed in the previous sections. The calculations with the decently-accurate CO-1 basis set are 10 to 40 times faster than the corresponding grid calculations.<sup>97</sup> In the  $\text{Ag}_{147}$  cluster the speed-ups are in most cases larger than in the smaller  $\text{Ag}_{55}$  system. This is because the studied systems are relatively small for the LCAO mode but relatively large for the grid mode, *i.e.*, when doubling the number of processors from 48 to 96, the grid mode has excellent scaling, whereas for the LCAO mode the benefit from the larger number of processors is minor, especially for the small  $\text{Ag}_{55}$ . Thus, the speed-up factors are expected to be even higher when the system size is further increased and the LCAO mode is able to fully take advantage of all the available processors.<sup>25</sup>

In addition to the number of basis functions, the computational performance is greatly affected also by the

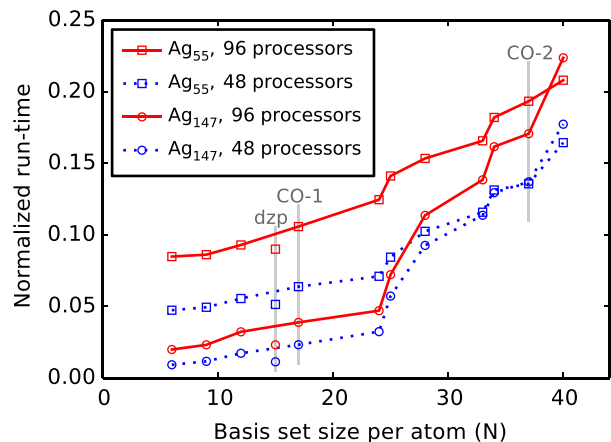


FIG. 6. Time-propagation run-time of the generated basis set series, shown for the  $\text{Ag}_{55}$  and  $\text{Ag}_{147}$  clusters calculated with 48 and 96 processors (cores). The run-time of the default dzp basis set is shown for comparison. The run-times have been normalized to the run-times of the corresponding grid references calculated with the indicated number of processors.



spatial extent of the basis functions. The default dzp basis set does not include diffuse functions that are important for describing the plasmonic response, leading to smaller run-time than the CO basis sets of similar size. Within the generated basis set series, the effect of basis function extent is seen as a staircase-like behavior in Fig. 6. For example, the addition of the f-type NGTO (*i.e.*, 7 additional basis functions per atom) increases the computational time only slightly, because the added functions are short-ranged. On the other hand, the addition of the diffuse s- or p-type NGTO (*i.e.*, 1 or 3 basis functions per atom, respectively) affects the computational time more clearly due to the functions' overlap with functions on nearby atoms. This effect is pronounced in the larger 147-atom cluster. More aggressive truncation of the NGTOs might yield better computational performance, but to ensure minimal deterioration in the accuracy, it may require re-optimization of the basis sets with the truncation explicitly taken into account in the CO routine.

## V. CONCLUSIONS

In this work, we have addressed the issue of basis set completeness in time-dependent density functional theory calculations. We have presented the extension of the completeness-optimization paradigm to the generation of hybrid NAO+NGTO basis sets, and used it to parametrize high-accuracy basis sets for nanoplasmonics calculations. We have demonstrated the performance of the scheme for the coinage metals Cu, Ag, and Au, which are experimentally interesting but computationally challenging due to their semi-core d-electrons that need to be modeled in simulations. We have shown that the generated basis sets are transferable to simulations of various metal nanoparticles and nanoalloys as well as to diverse xc functionals.

The results presented in this work are already promising, but further improvements of the scheme are still possible. For instance, the error metric used in the present work may not be optimal. The metric does not discriminate between different excitations, looking only at the aggregate intensity. This may result in spuriously small error values due to interference of different excitations. The use of an error metric that examines the convergence of the excitations one by one might yield even better basis set series.

Another approach deserving further development would be to revise the reference systems against which the basis sets are optimized. In the present work, accurate and systematically improving basis sets were obtained by optimizing the basis sets for homoatomic metal atom dimers. The generated sets were demonstrated to be transferable to larger as well as heterogeneous systems. However, it might be interesting to optimize basis sets for extended systems, instead. In a dimer, both atoms are "on the surface", which results in the generation

of diffuse functions to model the exponentially decaying density tails. In the solid state there is no exponential decay, and diffuse functions are often unnecessary. Nevertheless, our results indicate that the dynamical response is sufficiently captured already by the dimer for plasmonics calculations in larger nanoparticles.

The main advantage of the LCAO approach is that satisfactory results can be obtained much faster than with, *e.g.*, grid-type approaches. The main problem of the LCAO approach with NAOs (compared to GTO basis sets of quantum chemistry) has been the scarcity of systematically better basis sets. This issue has been addressed in the present work.

Although used here for nanoplasmonics, the completeness-optimization approach is completely general, being applicable to any property at any level of theory, also beyond DFT (see, *e.g.*, Refs. 43 and 58). For this reason we expect this approach to be widely useful in materials modeling by electronic structure methods, allowing for large-scale simulations with better control on their accuracy.

## VI. ACKNOWLEDGMENTS

We thank Ask H. Larsen for fruitful discussions. T.P.R. and S.L. acknowledge financial support from the Vilho, Yrjö and Kalle Väisälä Foundation. S.L. also acknowledges the Magnus Ehrnrooth Foundation for financial support. We thank the Academy of Finland for support through its Centres of Excellence Programme (2012–2017) under Project No. 251748 and through its FiDiPro Programme under Project No. 263294. We acknowledge the computational resources provided by the Aalto Science-IT project and CSC – IT Center for Science Ltd. (Espoo, Finland).

- <sup>1</sup>J. N. Anker, W. P. Hall, O. Lyandres, N. C. Shah, J. Zhao, and R. P. Van Duyne, *Nat. Mater.* **7**, 442 (2008).
- <sup>2</sup>J. A. Schuller, E. S. Barnard, W. Cai, Y. C. Jun, J. S. White, and M. L. Brongersma, *Nat. Mater.* **9**, 193 (2010).
- <sup>3</sup>H. A. Atwater and A. Polman, *Nat. Mater.* **9**, 205 (2010).
- <sup>4</sup>N. J. Halas, S. Lal, W.-S. Chang, S. Link, and P. Nordlander, *Chem. Rev.* **111**, 3913 (2011).
- <sup>5</sup>K. J. Savage, M. M. Hawkeye, R. Esteban, A. G. Borisov, J. Aizpurua, and J. J. Baumberg, *Nature* **491**, 574 (2012).
- <sup>6</sup>J. A. Scholl, A. L. Koh, and J. A. Dionne, *Nature* **483**, 421 (2012).
- <sup>7</sup>H. Haberland, *Nature* **494**, E1 (2013).
- <sup>8</sup>J. A. Scholl, A. García-Etxarri, A. L. Koh, and J. A. Dionne, *Nano Lett.* **13**, 564 (2013).
- <sup>9</sup>S. F. Tan, L. Wu, J. K. Yang, P. Bai, M. Bosman, and C. A. Nijhuis, *Science* **343**, 1496 (2014).
- <sup>10</sup>E. Runge and E. K. U. Gross, *Phys. Rev. Lett.* **52**, 997 (1984).
- <sup>11</sup>W. Ekardt, *Phys. Rev. Lett.* **52**, 1925 (1984).
- <sup>12</sup>M. J. Puska, R. M. Nieminen, and M. Manninen, *Phys. Rev. B* **31**, 3486 (1985).
- <sup>13</sup>J. Zuloaga, E. Prodan, and P. Nordlander, *Nano Lett.* **9**, 887 (2009).
- <sup>14</sup>J. Zuloaga, E. Prodan, and P. Nordlander, *ACS Nano* **4**, 5269 (2010).
- <sup>15</sup>P. Zhang, J. Feist, A. Rubio, P. García-González, and F. J. García-Vidal, *Phys. Rev. B* **90**, 161407 (2014).

- <sup>16</sup>C. Kumara and A. Dass, *Nanoscale* **3**, 3064 (2011).
- <sup>17</sup>A. C. Dharmaratne and A. Dass, *Chem. Commun.* **50**, 1722 (2014).
- <sup>18</sup>L. Serra and A. Rubio, *Phys. Rev. Lett.* **78**, 1428 (1997).
- <sup>19</sup>C. M. Aikens, S. Li, and G. C. Schatz, *J. Phys. Chem. C* **112**, 11272 (2008).
- <sup>20</sup>M. Stener, A. Nardelli, R. De Francesco, and G. Fronzoni, *J. Phys. Chem. C* **111**, 11862 (2007).
- <sup>21</sup>E. B. Guidez and C. M. Aikens, *J. Phys. Chem. C* **117**, 12325 (2013).
- <sup>22</sup>G. Piccini, R. W. A. Havenith, R. Broer, and M. Stener, *J. Phys. Chem. C* **117**, 17196 (2013).
- <sup>23</sup>G.-T. Bae and C. M. Aikens, *J. Phys. Chem. C* **116**, 10356 (2012).
- <sup>24</sup>G. Barcaro, L. Sementa, A. Fortunelli, and M. Stener, *J. Phys. Chem. C* **118**, 12450 (2014).
- <sup>25</sup>M. Kuisma, A. Sakko, T. P. Rossi, A. H. Larsen, J. Enkovaara, L. Lehtovaara, and T. T. Rantala, *Phys. Rev. B* **91**, 115431 (2015).
- <sup>26</sup>X. López-Lozano, H. Barron, C. Mottet, and H.-C. Weissker, *Phys. Chem. Chem. Phys.* **16**, 1820 (2014).
- <sup>27</sup>H.-C. Weissker and C. Mottet, *Phys. Rev. B* **84**, 165443 (2011).
- <sup>28</sup>X. López-Lozano, C. Mottet, and H.-C. Weissker, *J. Phys. Chem. C* **117**, 3062 (2013).
- <sup>29</sup>G. Barcaro, M. Broyer, N. Durante, A. Fortunelli, and M. Stener, *J. Phys. Chem. C* **115**, 24085 (2011).
- <sup>30</sup>E. B. Guidez and C. M. Aikens, *Nanoscale* **4**, 4190 (2012).
- <sup>31</sup>M.-S. Liao, P. Bonifassi, J. Leszczynski, P. C. Ray, M.-J. Huang, and J. D. Watts, *J. Phys. Chem. A* **114**, 12701 (2010).
- <sup>32</sup>E. B. Guidez, V. Mäkinen, H. Häkkinen, and C. M. Aikens, *J. Phys. Chem. C* **116**, 20617 (2012).
- <sup>33</sup>H.-C. Weissker, H. B. Escobar, V. D. Thanthirige, K. Kwak, D. Lee, G. Ramakrishna, R. L. Whetten, and X. López-Lozano, *Nat. Commun.* **5**, 3785 (2014).
- <sup>34</sup>S. Malola, L. Lehtovaara, J. Enkovaara, and H. Häkkinen, *ACS Nano* **7**, 10263 (2013).
- <sup>35</sup>S. Malola, L. Lehtovaara, and H. Häkkinen, *J. Phys. Chem. C* **118**, 20002 (2014).
- <sup>36</sup>L. Gell, L. Lehtovaara, and H. Häkkinen, *J. Phys. Chem. A* **118**, 8351 (2014).
- <sup>37</sup>G.-T. Bae and C. M. Aikens, *J. Phys. Chem. A* **116**, 8260 (2012).
- <sup>38</sup>F. Jensen, *WIREs Comput. Mol. Sci.* **3**, 273 (2013).
- <sup>39</sup>M. Miura, Y. Aoki, and B. Champagne, *J. Chem. Phys.* **127**, 084103 (2007).
- <sup>40</sup>D. P. Chong, *Can. J. Chem.* **73**, 79 (1995).
- <sup>41</sup>P. Manninen and J. Vaara, *J. Comput. Chem.* **27**, 434 (2006).
- <sup>42</sup>J. Lehtola, P. Manninen, M. Hakala, and K. Hämäläinen, *J. Chem. Phys.* **137**, 104105 (2012).
- <sup>43</sup>S. Lehtola, *J. Comput. Chem.* **36**, 335 (2015).
- <sup>44</sup>A. Tsolakidis, D. Sánchez-Portal, and R. M. Martin, *Phys. Rev. B* **66**, 235416 (2002).
- <sup>45</sup>S. Ikäläinen, P. Lantto, P. Manninen, and J. Vaara, *Phys. Chem. Chem. Phys.* **11**, 11404 (2009).
- <sup>46</sup>P. Lantto, K. Jackowski, W. Makulski, M. Olejniczak, and M. Jaszuński, *J. Phys. Chem. A* **115**, 10617 (2011).
- <sup>47</sup>J. Vähäkangas, S. Ikäläinen, P. Lantto, and J. Vaara, *Phys. Chem. Chem. Phys.* **15**, 4634 (2013).
- <sup>48</sup>N. Abuzaid, A. M. Kantola, and J. Vaara, *Mol. Phys.* **111**, 1390 (2013).
- <sup>49</sup>M. Jaszuński and M. Olejniczak, *Mol. Phys.* **111**, 1355 (2013).
- <sup>50</sup>J. Vaara, M. Hanni, and J. Jokisaari, *J. Chem. Phys.* **138**, 104313 (2013).
- <sup>51</sup>S. Ikäläinen, P. Lantto, P. Manninen, and J. Vaara, *J. Chem. Phys.* **129**, 124102 (2008).
- <sup>52</sup>S. Ikäläinen, M. V. Romalis, P. Lantto, and J. Vaara, *Phys. Rev. Lett.* **105**, 153001 (2010).
- <sup>53</sup>S. Ikäläinen, P. Lantto, and J. Vaara, *J. Chem. Theory Comput.* **8**, 91 (2012).
- <sup>54</sup>T. S. Pennanen, S. Ikäläinen, P. Lantto, and J. Vaara, *J. Chem. Phys.* **136**, 184502 (2012).
- <sup>55</sup>J. Shi, S. Ikäläinen, J. Vaara, and M. V. Romalis, *J. Phys. Chem. Lett.* **4**, 437 (2013).
- <sup>56</sup>L.-J. Fu and J. Vaara, *J. Chem. Phys.* **138**, 204110 (2013).
- <sup>57</sup>J. Vähäkangas, P. Lantto, and J. Vaara, *J. Phys. Chem. C* **118**, 23996 (2014).
- <sup>58</sup>S. Lehtola, P. Manninen, M. Hakala, and K. Hämäläinen, *J. Chem. Phys.* **138**, 044109 (2013).
- <sup>59</sup>P. Hohenberg and W. Kohn, *Phys. Rev.* **136**, B864 (1964).
- <sup>60</sup>W. Kohn and L. J. Sham, *Phys. Rev.* **140**, A1133 (1965).
- <sup>61</sup>M. A. L. Marques, N. T. Maitra, F. M. S. Nogueira, E. K. U. Gross, and A. Rubio, eds., *Fundamentals of Time-Dependent Density Functional Theory*, Lecture Notes in Physics, Vol. 837 (Springer, 2012).
- <sup>62</sup>K. Yabana and G. F. Bertsch, *Phys. Rev. B* **54**, 4484 (1996).
- <sup>63</sup>M. E. Casida, in *Recent Advances in Density Functional Methods, Part I*, edited by D. P. Chong (World Scientific, Singapore, 1995) p. 155.
- <sup>64</sup>J. J. Mortensen, L. B. Hansen, and K. W. Jacobsen, *Phys. Rev. B* **71**, 035109 (2005).
- <sup>65</sup>M. Walter, H. Häkkinen, L. Lehtovaara, M. Puska, J. Enkovaara, C. Rostgaard, and J. J. Mortensen, *J. Chem. Phys.* **128**, 244101 (2008).
- <sup>66</sup>A. H. Larsen, M. Vanin, J. J. Mortensen, K. S. Thygesen, and K. W. Jacobsen, *Phys. Rev. B* **80**, 195112 (2009).
- <sup>67</sup>“GPAW: DFT and beyond within the projector-augmented wave method,” <https://wiki.fysik.dtu.dk/gpaw/>.
- <sup>68</sup>J. Enkovaara, C. Rostgaard, J. J. Mortensen, J. Chen, M. Dulak, L. Ferrighi, J. Gavnholt, C. Glinsvad, V. Haikola, H. A. Hansen, H. H. Kristoffersen, M. Kuisma, A. H. Larsen, L. Lehtovaara, M. Ljungberg, O. Lopez-Acevedo, P. G. Moses, J. Ojanen, T. Olsen, V. Petzold, N. A. Romero, J. Stausholm-Møller, M. Strange, G. A. Tritsarlis, M. Vanin, M. Walter, B. Hammer, H. Häkkinen, G. K. H. Madsen, R. M. Nieminen, J. K. Nørskov, M. Puska, T. T. Rantala, J. Schiøtz, K. S. Thygesen, and K. W. Jacobsen, *J. Phys.: Condens. Matter* **22**, 253202 (2010).
- <sup>69</sup>S. Bahn and K. Jacobsen, *Comput. Sci. Eng.* **4**, 56 (2002).
- <sup>70</sup>P. E. Blöchl, *Phys. Rev. B* **50**, 17953 (1994).
- <sup>71</sup>P. Pyykkö, *Annu. Rev. Phys. Chem.* **63**, 45 (2012).
- <sup>72</sup>J. Lehtola, M. Hakala, A. Sakko, and K. Hämäläinen, *J. Comput. Chem.* **33**, 1572 (2012).
- <sup>73</sup>S. Lehtola, “ERKALE — HF/DFT from Hel,” (2014), <http://erkale.googlecode.com>.
- <sup>74</sup>J. M. Soler, E. Artacho, J. D. Gale, A. García, J. Junquera, P. Ordejón, and D. Sánchez-Portal, *J. Phys.: Condens. Matter* **14**, 2745 (2002).
- <sup>75</sup>V. Blum, R. Gehrke, F. Hanke, P. Havu, V. Havu, X. Ren, K. Reuter, and M. Scheffler, *Comput. Phys. Commun.* **180**, 2175 (2009).
- <sup>76</sup>X. Ren, P. Rinke, V. Blum, J. Wieferink, A. Tkatchenko, A. Sanfilippo, K. Reuter, and M. Scheffler, *New J. Phys.* **14**, 053020 (2012).
- <sup>77</sup>I. Y. Zhang, X. Ren, P. Rinke, V. Blum, and M. Scheffler, *New J. Phys.* **15**, 123033 (2013).
- <sup>78</sup>F. Corsetti, M.-V. Fernández-Serra, J. M. Soler, and E. Artacho, *J. Phys.: Condens. Matter* **25**, 435504 (2013).
- <sup>79</sup>This NGTO construction scheme is readily available in GPAW.
- <sup>80</sup>These conditions are equivalent to restricting Gaussian exponents to following limits: s-shell: 0.0090–0.93, p-shell: 0.014–1.4, d-shell: 0.019–1.9, f-shell: 0.024–2.4.
- <sup>81</sup>J. P. Perdew, K. Burke, and M. Ernzerhof, *Phys. Rev. Lett.* **77**, 3865 (1996).
- <sup>82</sup>J. P. Perdew, K. Burke, and M. Ernzerhof, *Phys. Rev. Lett.* **78**, 1396 (1997).
- <sup>83</sup>A. Castro, A. Rubio, and M. J. Stott, *Can. J. Phys.* **81**, 1151 (2003).
- <sup>84</sup>J. R. Lombardi and B. Davis, *Chem. Rev.* **102**, 2431 (2002).
- <sup>85</sup>See supplemental material at <http://dx.doi.org/10.1063/1.4913739> for the generated NAO-sz+NGTO basis sets and the relaxed nanoparticle geometries.

- <sup>86</sup>P. A. M. Dirac, *Math. Proc. Cambridge Philos. Soc.* **26**, 376 (1930).
- <sup>87</sup>F. Bloch, *Z. Angew. Phys.* **57**, 545 (1929).
- <sup>88</sup>J. P. Perdew and Y. Wang, *Phys. Rev. B* **45**, 13244 (1992).
- <sup>89</sup>A. D. Becke, *Phys. Rev. A* **38**, 3098 (1988).
- <sup>90</sup>C. Lee, W. Yang, and R. G. Parr, *Phys. Rev. B* **37**, 785 (1988).
- <sup>91</sup>B. Miehlich, A. Savin, H. Stoll, and H. Preuss, *Chem. Phys. Lett.* **157**, 200 (1989).
- <sup>92</sup>O. Gritsenko, R. van Leeuwen, E. van Lenthe, and E. J. Baerends, *Phys. Rev. A* **51**, 1944 (1995).
- <sup>93</sup>M. Kuisma, J. Ojanen, J. Enkovaara, and T. T. Rantala, *Phys. Rev. B* **82**, 115106 (2010).
- <sup>94</sup>J. Yan, K. W. Jacobsen, and K. S. Thygesen, *Phys. Rev. B* **84**, 235430 (2011).
- <sup>95</sup>J. Yan, K. W. Jacobsen, and K. S. Thygesen, *Phys. Rev. B* **86**, 241404 (2012).
- <sup>96</sup>Timings were performed on Intel Xeon E5-2680 v2 processors with FDR InfiniBand interconnect.
- <sup>97</sup>The exact speed-up factors are likely to be affected by the choice between the different parallelization schemes.